Supplementary Information

Growth of High-Quality Semiconducting Tellurium Films for High-Performance p-channel Field-Effect Transistors with Wafer-Scale Uniformity

Taikyu Kim[1], Cheol Hee Choi[1], Pilgyu Byeon[2], Miso Lee[3], Aeran Song[4], Kwun-Bum Chung[4], Seungwu Han[3], Sung-Yoon Chung[2], Kwon-Shik Park[5], and Jae Kyeong Jeong[1]*

[1]Department of Electronic Engineering, Hanyang University, Seoul 04763, Republic of Korea

[2]Department of Materials Science & Engineering, Korea Advanced Institute of Science & Technology, Daejeon 34141, Republic of Korea

[3]Department of Materials Science and Engineering and Research Institute of Advanced Materials, Seoul National University, Seoul 08826, Republic of Korea

[4]Division of Physics and Semiconductor Science, Dongguk University, Seoul 04620, Republic of Korea

[5]R&D Center, LG Display Company, Paju-Si, Kyonggi-Do 413-791, Republic of Korea

Email: jkjeong1@hanyang.ac.kr

Supplementary Note 1

Crystal growth mechanism through interfacial energy stabilization To elucidate the growth of the hexagonal Te crystal in the partially oxidized Te film, let us consider the formation of a hexagonal Te crystal embryo in the amorphous phase. With the premise that a crystal embryo is spherical for simplicity, the free energy difference for crystal growth consists mainly of two parts: one comes from the interfacial energy and the other from the free energy difference per unit volume[1]. The free energy difference (ΔG_r) is given by[1]

$$\Delta G_r = 4\pi r^2 \gamma + \frac{4}{3}\pi r^3 \Delta G_v \tag{1}$$

where r is the radius of the embryo, γ is the interfacial energy, and ΔG_v is the free energy difference per unit volume for the phase transition. The distortion energy term derived from the oxidation must be added to the right side[2]. Considering the previous experimental study on the Ellingham diagram[3], however, oxygen within the Te-based amorphous phase can diffuse into the Al_2O_3 encapsulation layer, enabling this term to be neglected. Deoxidization was also confirmed through X-ray photoelectron spectroscopy (XPS), which can be seen in the main text (**Figure 2a**). Therefore, the atomic distortion in the amorphous phase due to the oxidized states can be relieved through oxygen diffusion into the encapsulation layer, reducing the interfacial energy with the crystal embryo. From the relation $\partial(\Delta G_r)/\partial r = 0$, the critical radius ($r^*$) and free energy difference (ΔG^*) of the embryo are given by[1]

$$r^* = \frac{-2\gamma}{\Delta G_v} \tag{2}$$

$$\Delta G^* = \frac{4}{3}\pi r^{*2} \gamma = \frac{16\pi\gamma^3}{3(\Delta G_v)^2} \tag{3}$$

Thus, the reduced interfacial energy can decrease r^* and ΔG^*, promoting hexagonal Te crystal growth, as depicted in Supplementary Figure 1. The encapsulation layer also alleviates the surface energy that destabilizes the crystal growth in the film with a high surface-to-volume ratio[1], followed by an enhancement in the crystallinity. Furthermore, through polarized light

microscopy (PLM), the crystal domains are demonstrated to be enlarged with encapsulation (see **Figure 1** in the main text).

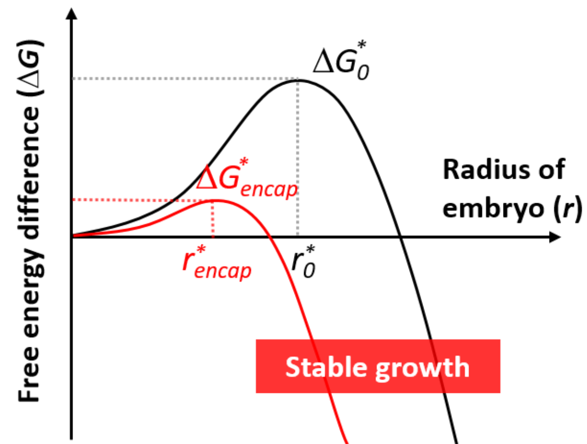

Supplementary Figure 1. Schematic plot of the crystal growth mechanism through interfacial energy stabilization.

Supplementary Note 2

First-principles calculation for p-type Te depending on the oxygen fraction The orbitals at the valence band (VB) edge are studied on the basis of density functional theory. In Supplementary Figure 2, we compare orbital characteristics between amorphous TeO (*a*-TeO) and amorphous TeO_2 (*a*-TeO_2). For *a*-TeO, Te-5p orbitals (yellow surfaces) are dominant at the VB edge, and they comprise conduction paths for holes, resulting in a low hole effective mass (Supplementary Figure 2a). This can also be confirmed by the band dispersion in Supplementary Figure 15b. In contrast, the VB edges of *a*-TeO_2 consist of localized O-2p orbitals (Supplementary Figure 2b), which increases the hole effective mass. For further insight into orbital properties that depend on the O/Te ratio, *a*-TeO_x structures ($1 \leq x \leq 2$) were examined. The Te-p orbitals are dominant at the VB edge, suggesting that p-type characteristics are retained, when x is less than 1.8 (Supplementary Figure 3,4).

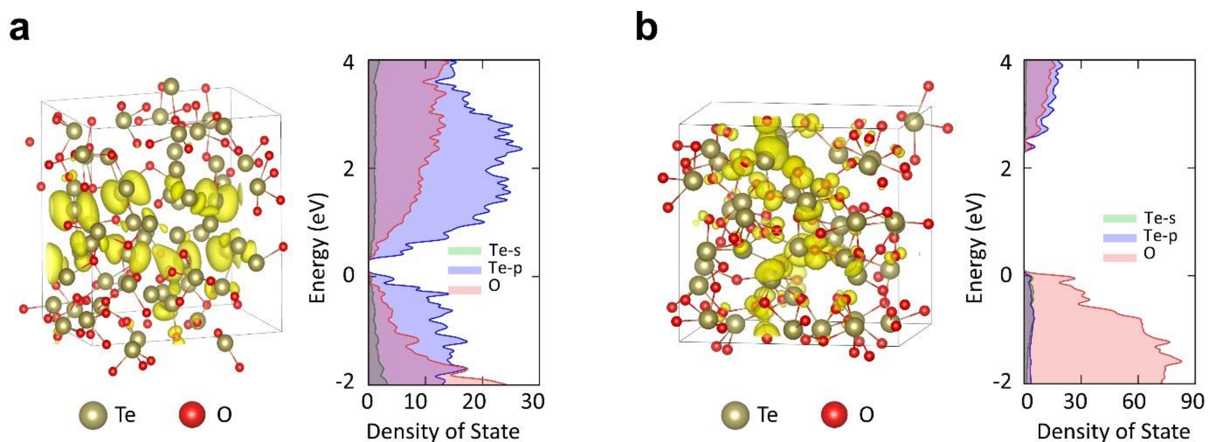

Supplementary Figure 2. Density functional theory calculation results of the amorphous tellurium oxide (*a*-TeO_X) structure ($x = 1, 2$): Atomic configuration with the charge distribution at the valence band (*VB*) edge and density of state in (a) *a*-TeO and (b) *a*-TeO_2.

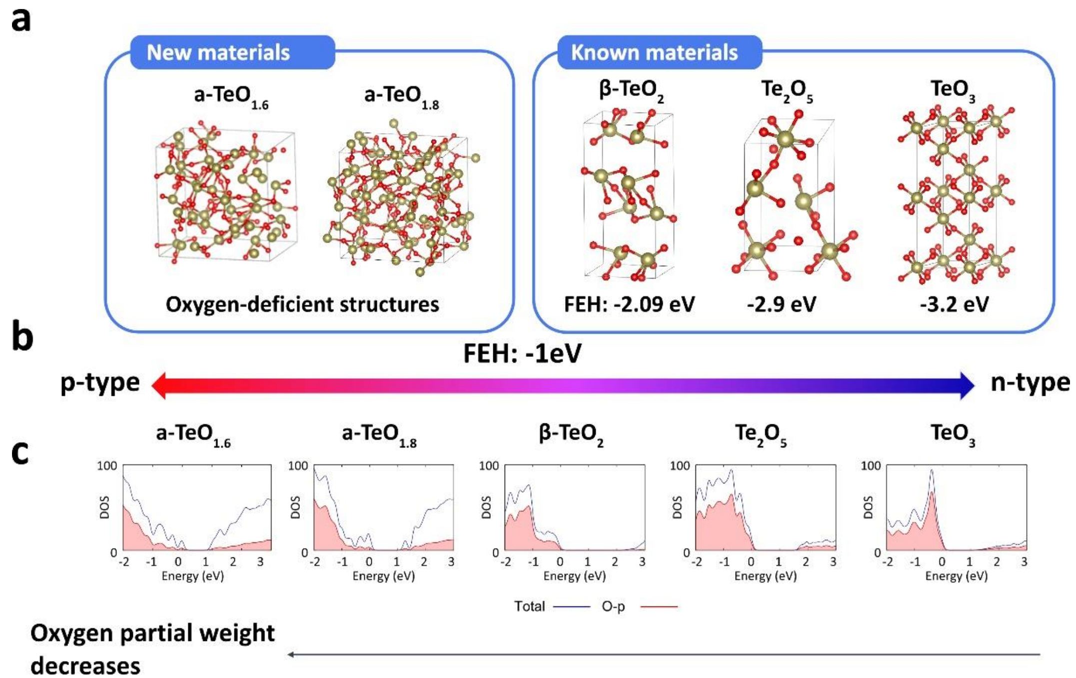

Supplementary Figure 3. Oxygen-dependent structural evolution in *a*-TeOx (1.6 ≤ x ≤ 3): (a) Atomic configurations. (b) Schematic diagram of the defect formation energy of interstitial hydrogen in the +1 charge state (H_i^+) with the Fermi level at the *VB* edge (henceforward referred to as FEH) depending on the *a*-TeO_X structure, which is an efficient descriptor for p-type dopability[4]. (c) Density of states.

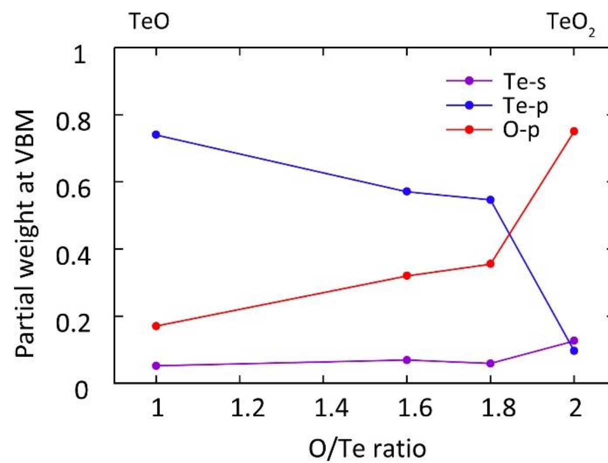

Supplementary Figure 4. Partial weight of orbitals at the *VB* edge depending on the O/Te molar ratio in the amorphous TeOx structure (1 ≤ x ≤ 2): TeO_X can exhibit p-type characteristics when O/Te ≤ 1.8 because Te-p orbitals dominate the *VB* edge.

Supplementary Figures

1. X-ray diffraction depending on the post deposition annealing temperature (T_A)

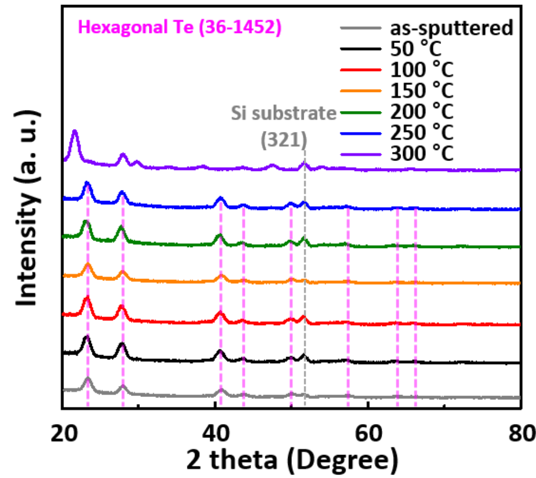

Supplementary Figure 5. X-ray diffraction (XRD) patterns of the sputtered Te films depending on the post deposition annealing temperature (T_A): an abrupt change in the crystalline structure at T_A = 300 °C was confirmed.

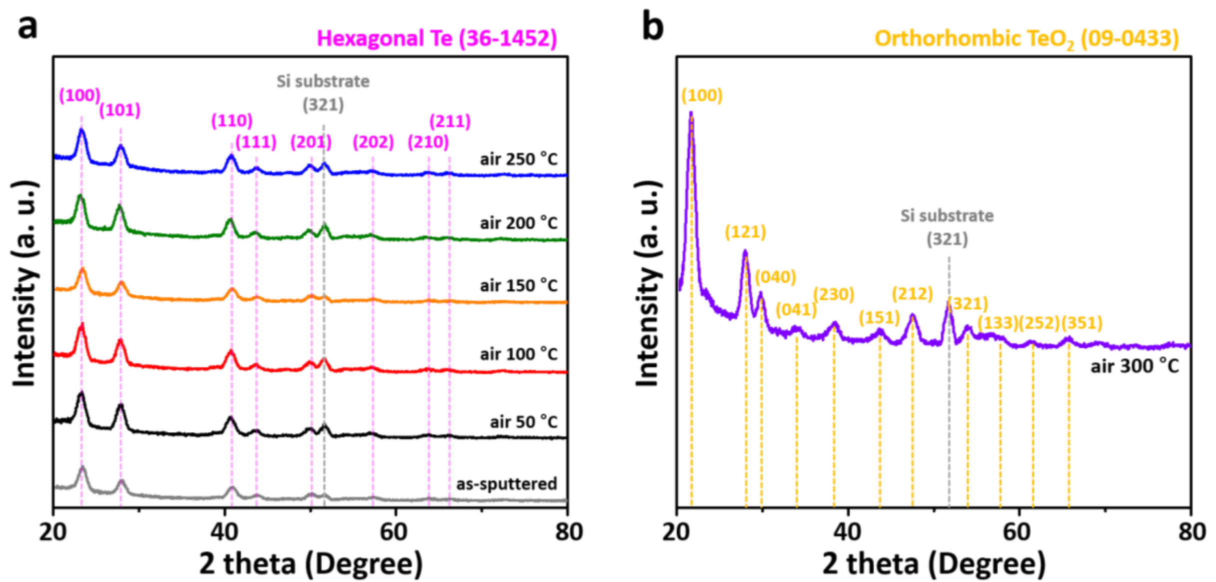

Supplementary Figure 6. Peak identification in the XRD patterns for the Te films: (a) T_A: ≤ 250 °C. (b) T_A = 300 °C.

2. Te volatilization detection

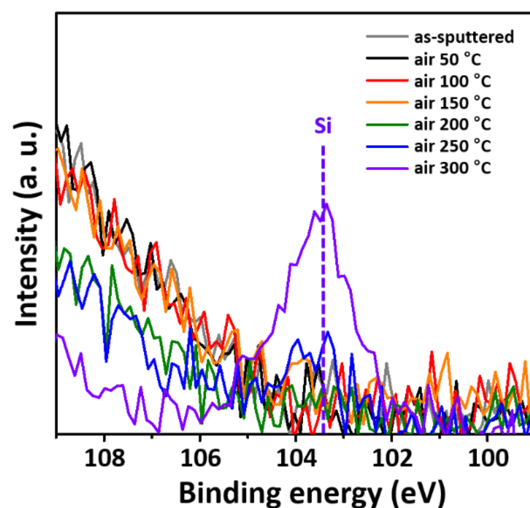

Supplementary Figure 7. Si *2p* peak in the XPS spectra of the sputtered Te films depending on T_A: a signal of Si from the Si/SiO_2 substrate was clearly shown due to Te volatilization.

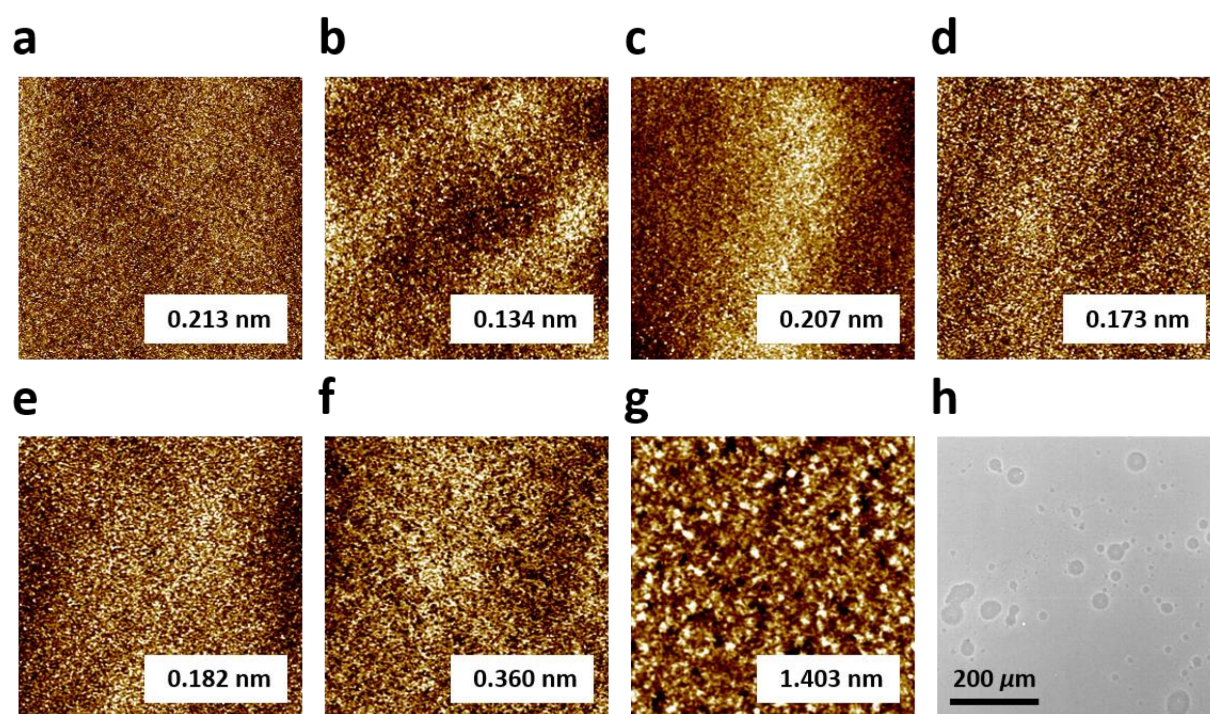

Supplementary Figure 8. Atomic force microscopy (AFM) and optical images of the sputtered Te films depending on T_A: (a) w/o annealing. (b-g) 50, 100, 150, 200, 250, and 300 °C-annealed films. The inset indicates the root-mean square surface roughness. (h) Optical image of the 300 °C-annealed Te film.

3. High-resolution transmission electron microscopy images

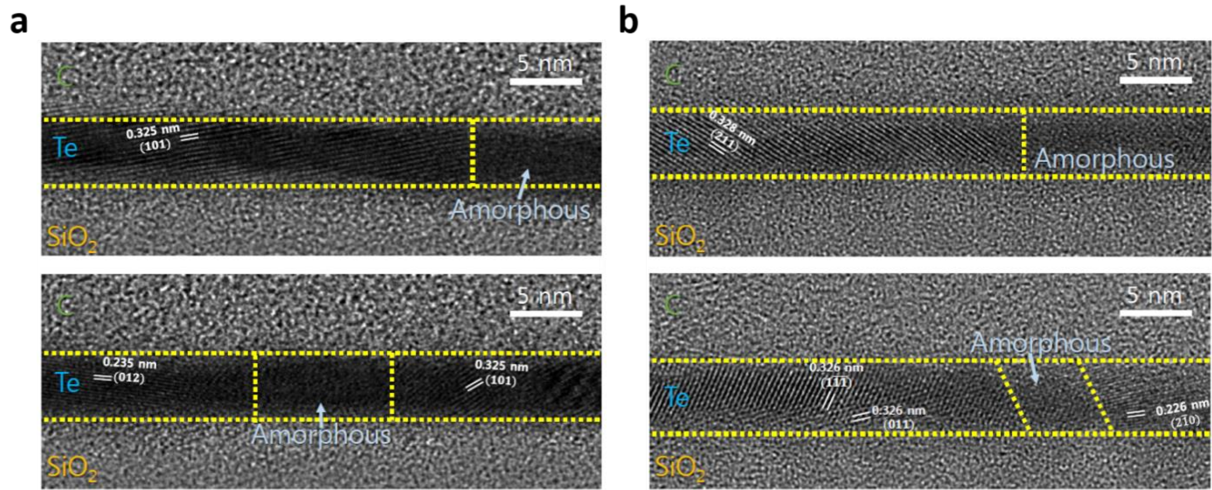

Supplementary Figure 9. High-resolution transmission electron microscopy (HRTEM) images of the sputtered Te films depending on T_A: (a) as-deposited film. (b) 150 °C-annealed film.

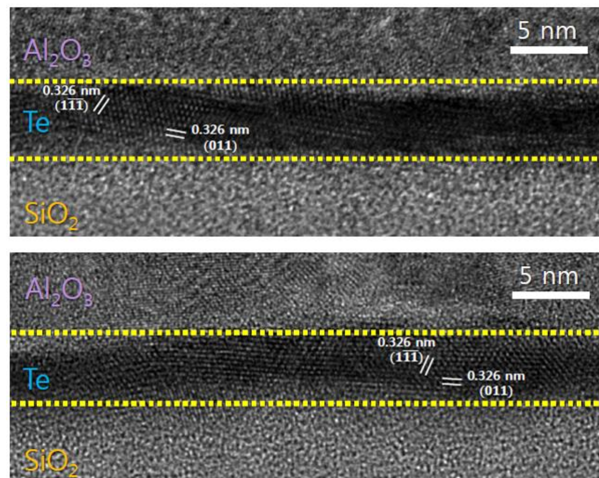

Supplementary Figure 10. HRTEM images of the encapsulated Te films.

4. X-ray photoelectron spectroscopy depending on T_A

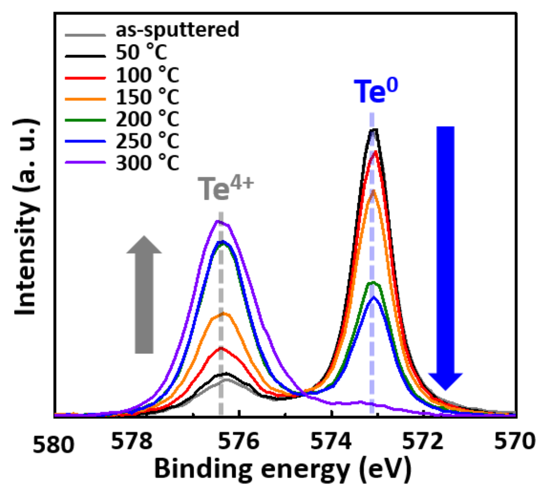

Supplementary Figure 11. Te $3d_{5/2}$ peak in the XPS spectra of the sputtered Te films depending on T_A.

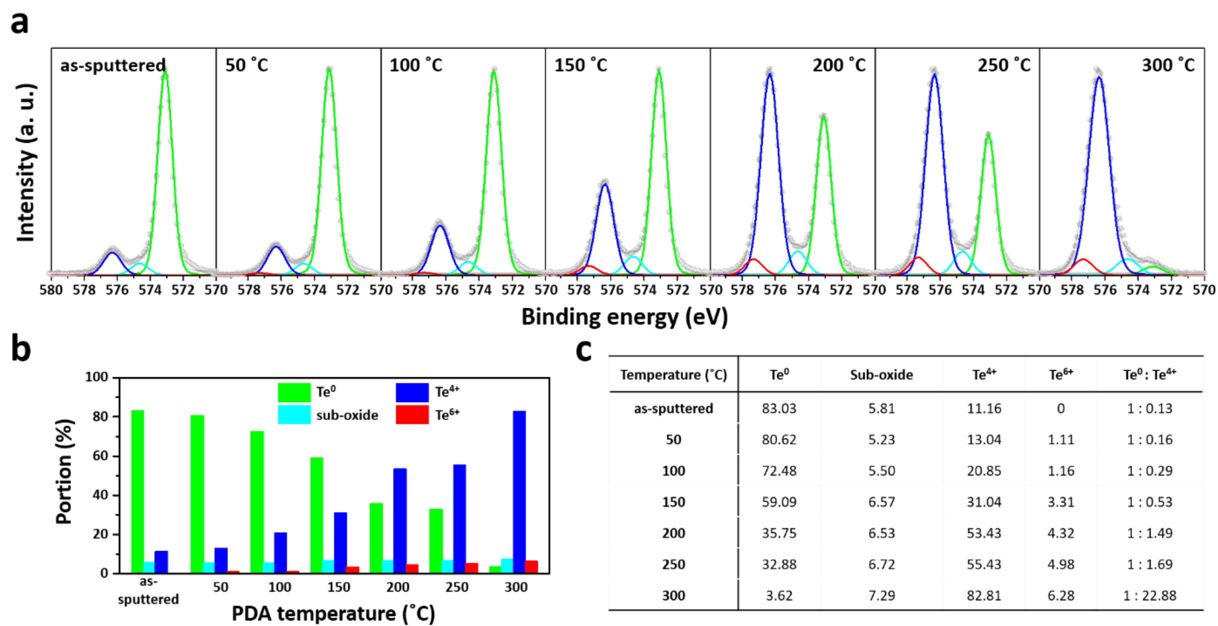

Temperature (˚C)	Te^0	Sub-oxide	Te^{4+}	Te^{6+}	Te^0 : Te^{4+}
as-sputtered	83.03	5.81	11.16	0	1 : 0.13
50	80.62	5.23	13.04	1.11	1 : 0.16
100	72.48	5.50	20.85	1.16	1 : 0.29
150	59.09	6.57	31.04	3.31	1 : 0.53
200	35.75	6.53	53.43	4.32	1 : 1.49
250	32.88	6.72	55.43	4.98	1 : 1.69
300	3.62	7.29	82.81	6.28	1 : 22.88

Supplementary Figure 12. XPS results of Te films with the different T_A: (a) Te $3d_{5/2}$ peak deconvolution. Summary of the deconvoluted chemical states of Te using (b) Column graph, and (c) Numerical format.

5. Optical characteristics depending on T_A

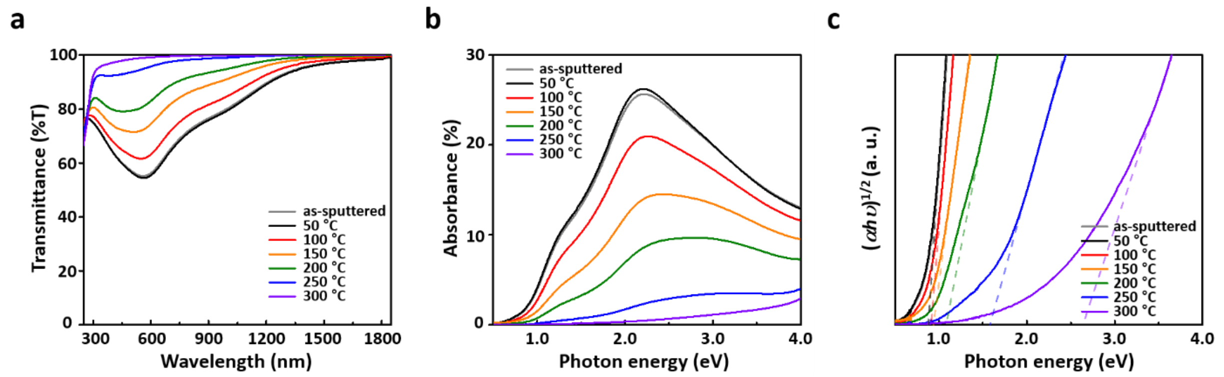

Supplementary Figure 13. Optical characteristics of the 4-nm-thick sputtered Te films depending on T_A: (a) Transmittance. (b) Absorbance. (c) Indirect bandgap extraction.

Supplementary Figure 14. Photograph of the 4-nm-thick sputtered Te films.

6. Raman spectroscopy depending on T_A

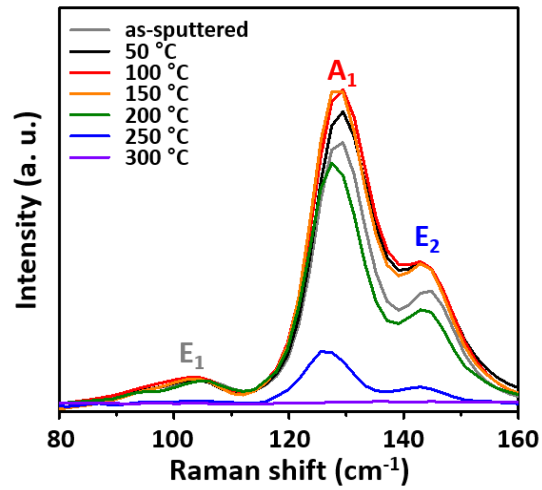

Supplementary Figure 15. Raman spectra of the sputtered Te films depending on T_A.

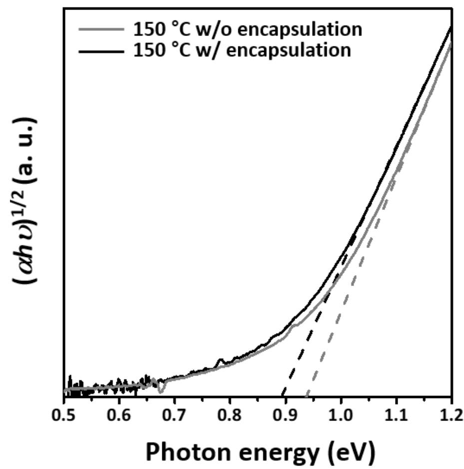

Supplementary Figure 16. Bandgap comparison of the 150 °C-annealed Te films depending on the strain effect through the encapsulation.

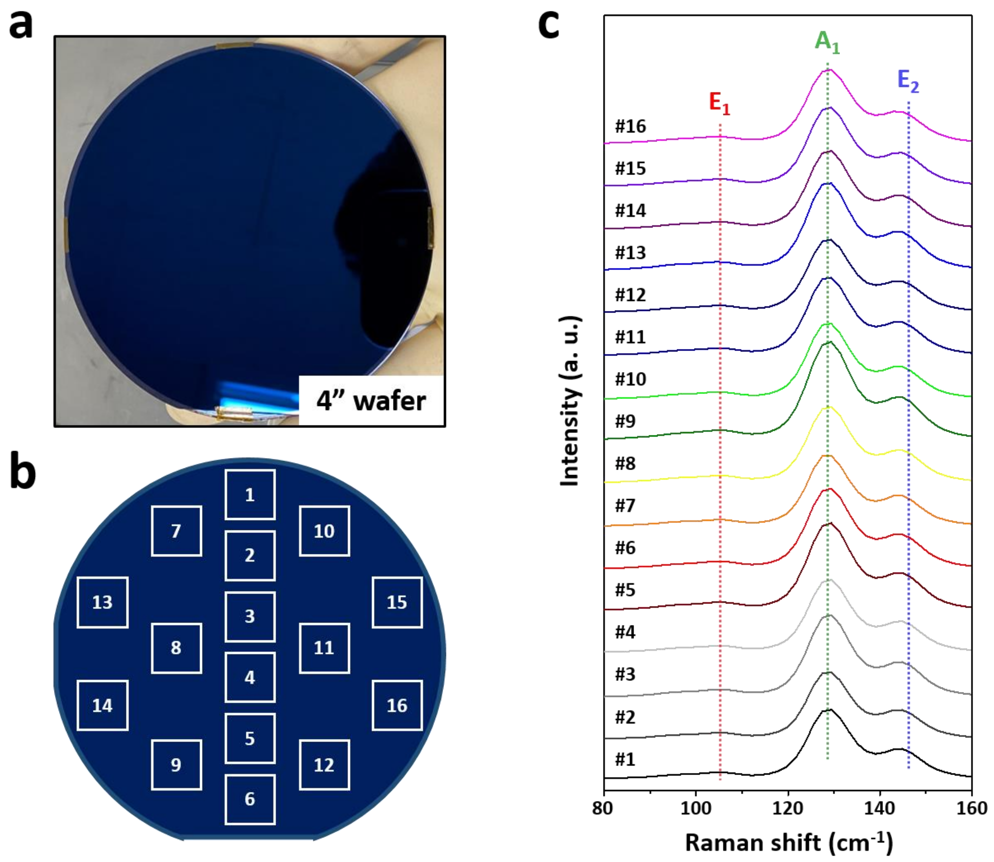

Supplementary Figure 17. Wafer-scale uniformity confirmation: (a) Photograph of the sputtered Te film on the 4-inch Si/SiO_2 wafer. (b) Schematic of the wafer indicating each measured location. (c) Raman spectra.

7. T_A-dependent electrical characteristics

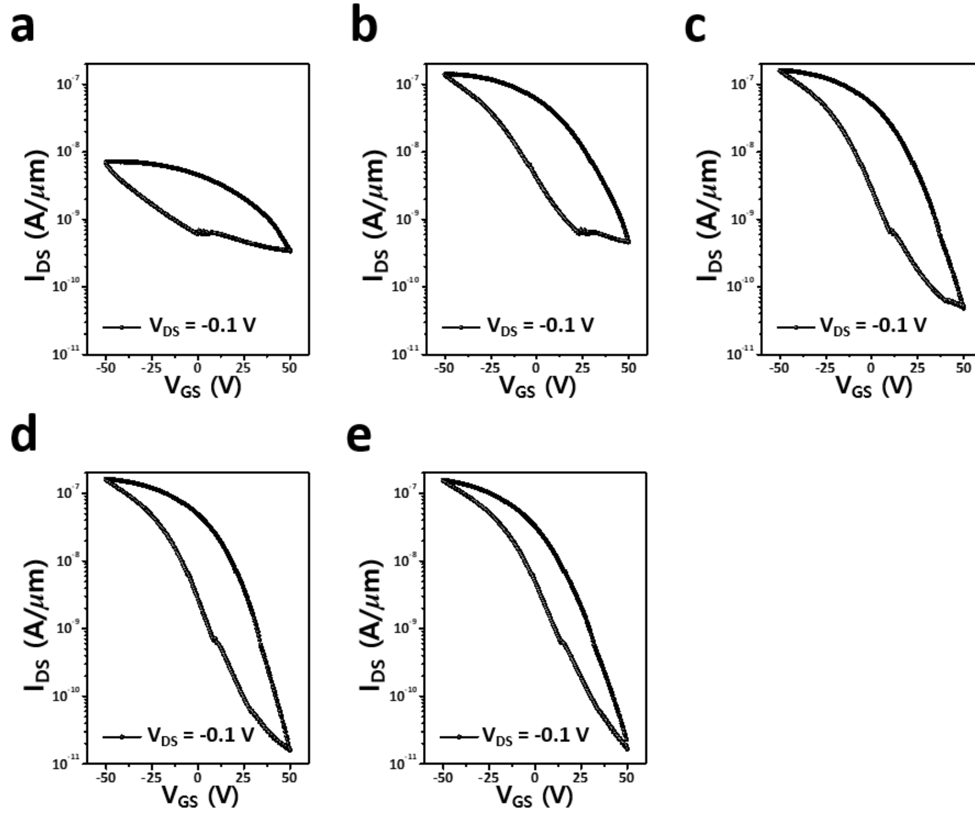

Supplementary Figure 18. T_A-dependent transfer characteristics of Te FETs: (a-e) w/o annealing and 50, 100, 150, and 200 °C-annealed FETs, showing that the device performance is enhanced up to 150 °C and degraded at 200 °C. At T_A > 200 °C, the Te FETs show resistive characteristics.

Supplementary Table 1. Device performance of Te FETs with different T_A.

T_A (°C)	μ_{FE} ($cm^2V^{-1}s^{-1}$)	$I_{ON/OFF}$	SS ($Vdec^{-1}$)
as-sputtered	4.8	2.1×10^1	31.0
50	50.2	3.1×10^2	14.0
100	51.8	3.4×10^3	11.8
150	52.5	1.0×10^4	10.2
200	46.0	9.4×10^3	12.5
250	N/A	N/A	N/A
300	N/A	N/A	N/A

8. Density functional theory calculation

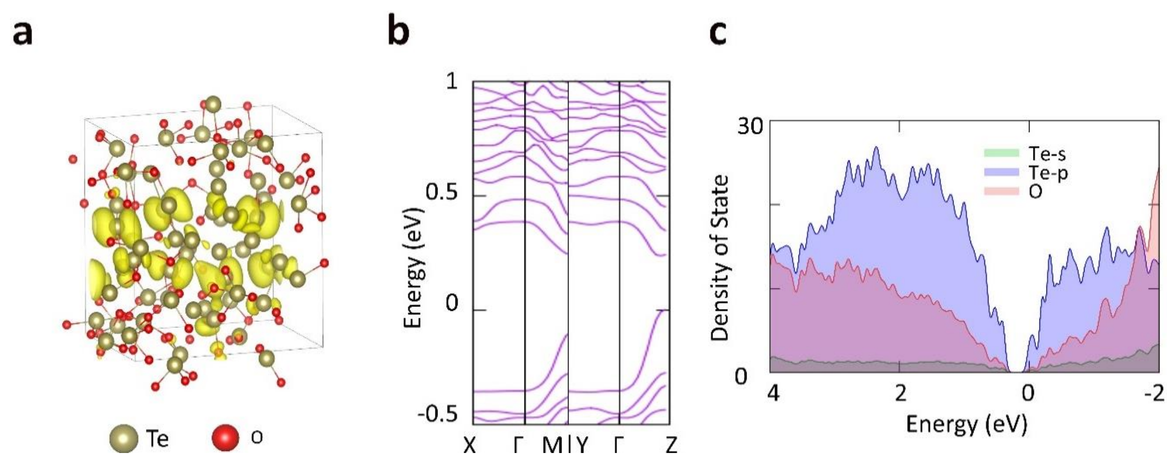

Supplementary Figure 19. Density functional theory calculation results of the amorphous TeO structure (O/Te ratio = 1): (a) Atomic configuration with the charge distribution at the *VB* edge. (b) Band structure. (c) Density of state (see details in Supplementary Note 2).

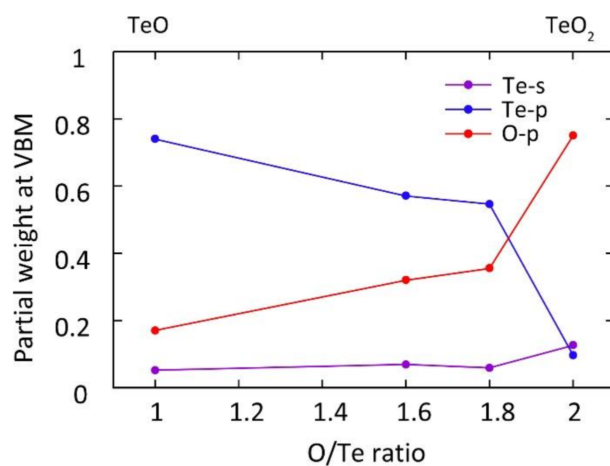

Supplementary Figure 20. Partial weight of orbitals at the *VB* edge depending on the O/Te molar ratio in the amorphous TeO_x structure ($1 \leq x \leq 2$): TeO_x can exhibit p-type characteristics when O/Te $\leq$ 1.8 because Te-p orbitals dominate the *VB* edge.

9. Air stability of Te FET annealed at 150 °C

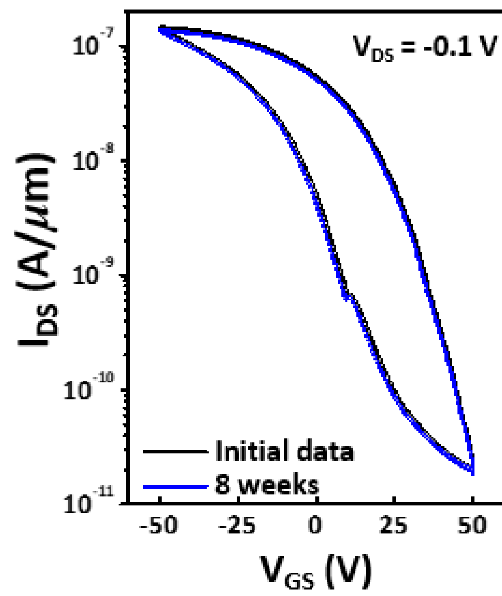

Supplementary Figure 21. Immunity of Te film against air exposure: Transfer characteristics of a Te FET annealed at 150 °C with stability measured for up to 8 weeks.

10. Effect of vacuum annealing at 150 °C

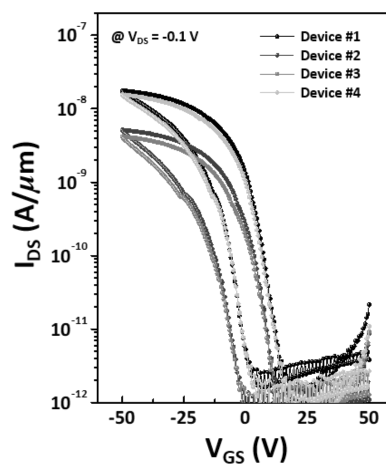

Supplementary Figure 22. Effect of vacuum annealing on the device performance: Transfer characteristics of encapsulated Te FETs using the channel layer annealed at 150 °C under vacuum ambience.

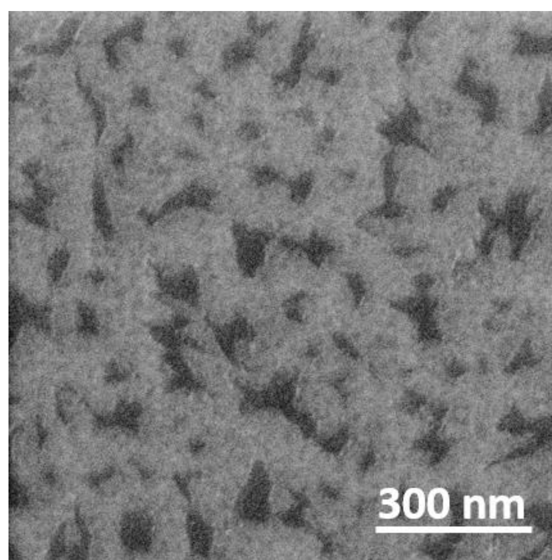

Supplementary Figure 23. Sublimation of Te by the vacuum annealing: Top view image of surface of Te film annealed at 150 °C under vacuum ambience through scanning electron microscopy.

11. Complementary metal oxide semiconductor inverter.

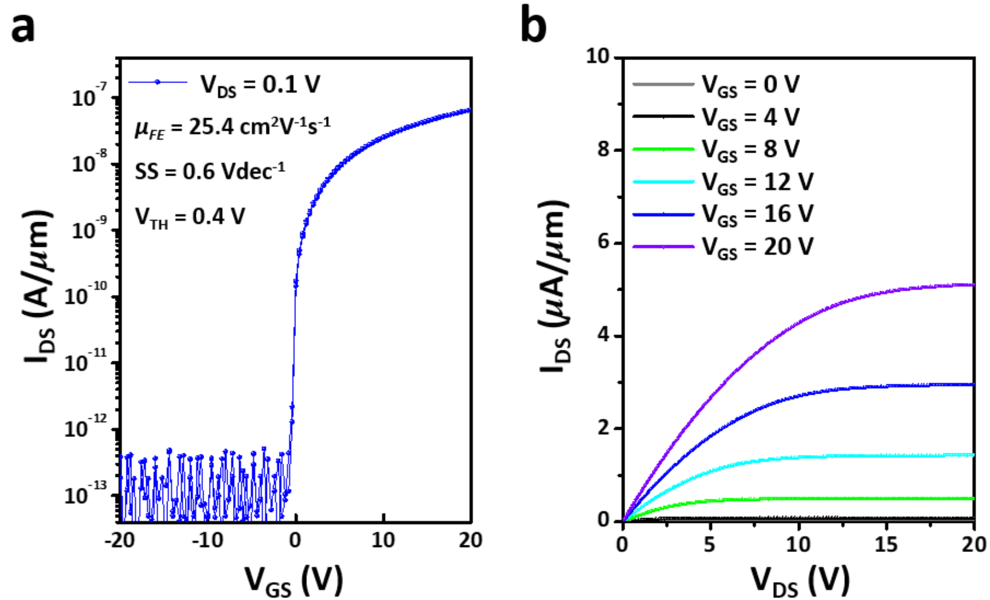

Supplementary Figure 24. Electrical characteristics of n-indium-gallium-zinc oxide (IGZO) FETs for complementary metal oxide semiconductor (CMOS) integration: (a) Transfer characteristics. (b) Output characteristics.

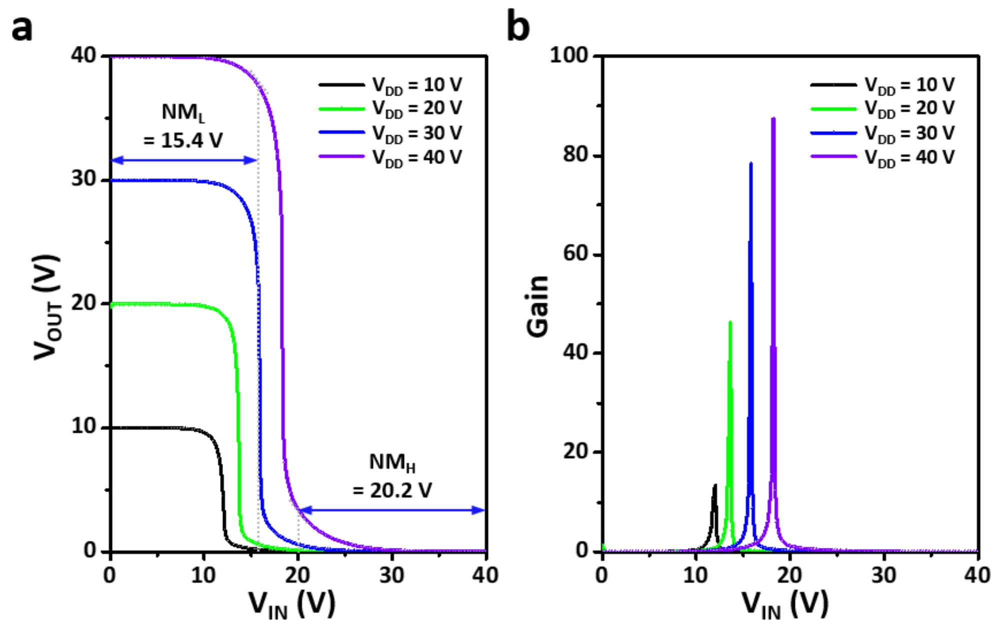

Supplementary Figure 25. Device performances of CMOS inverter using the encapsulated Te and IGZO FETs: (a) Voltage transfer characteristics. Dashed line indicates the noise margins extracted at the gain of -1. (b) Calculation of the voltage gain from the output swing.

12. Determination of the extracted values of μ_{FE}.

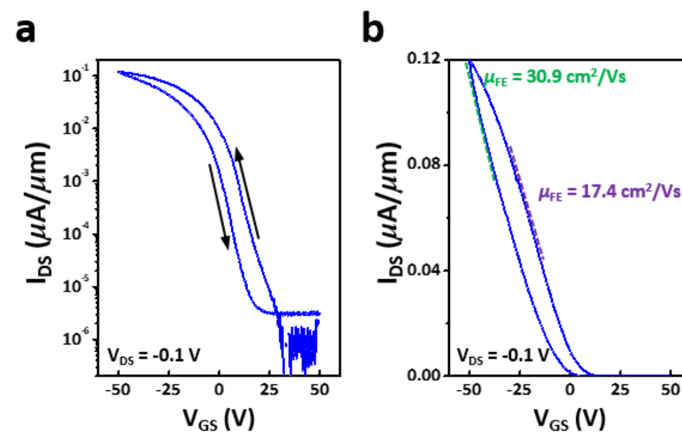

Supplementary Figure 26. Gate voltage sweep direction-dependent hysteresis-derived disparity in the field-effect mobility extraction of transfer characteristics of the encapsulated Te FET: (a) Semi-logarithmic curve. (b) Linear curve.

13. Device performance comparison

Supplementary Table 2. Device performances comparison of recently reported p-channel FETs.

Supplementary Ref.	Material	Thickness/Diameter (nm)	Mobility ($cm^2V^{-1}s^{-1}$)	$I_{ON/OFF}$	Fab. Methods	Fab. Temp.*) (°C)	Comments
[5]	BP	5	55	10^5	Exfoliation	1000	
[6]	BP	13	310	$10^3 \sim 10^4$	Exfoliation	-	
[7]	BP	5	286	$\sim10^4$	Exfoliation	-	
[8]	BP	1.9	~172	$\sim2.7 \times 10^4$	Exfoliation	-	Ambipolar
[9]	BP	4 ~ 8	95.6	$10^4 \sim 10^5$	Exfoliation	-	
[10]	BP	10	280	$\sim3 \times 10^3$	Exfoliation	-	
[11]	BP	15	~413	$\sim10^2$	Exfoliation	-	
[12]	$MoTe_2$	2.7	20	10^6	Exfoliation	1150	
[13]	$MoTe_2$	3.1	1	$\sim10^3$	CVD	700	
[14]	$MoTe_2$	2.1	0.03	2×10^3	Exfoliation	-	Ambipolar
[15]	$MoTe_2$	3.6	6	10^5	Exfoliation	-	
[16]	$MoTe_2$	11	41	$10^5 \sim 10^6$	Exfoliation	-	Ambipolar
[17]	MoS_2	10	68	$\sim10^7$	Exfoliation	-	$AuCl_3$ doping
[18]	MoS_2	~0.65	2.3	$>10^6$	Exfoliation	-	Molecular doping
[19]	MoS_2	3.5	36	$10^5 \sim 10^6$	Exfoliation	-	Nb doping; Estimated $I_{ON/OFF}$ based on the corresponding reference
[20]	WSe_2	8	100	$>10^7$	Exfoliation	-	
[21]	WSe_2	5	42.6	$\sim10^8$	Exfoliation		
[22]	WSe_2	~2	10	$\sim10^3$	Synthesis	800	Estimated $I_{ON/OFF}$ based on the corresponding reference
[23]	Cu_XO	30	0.7	1.2×10^4	Sputtering	RT	Ga doping
[24]	Cu_XO	150	1.4	4.1×10^6	PLD	RT	S treatment
[25]	Cu_XO	40	0.8	2.8×10^8	Sputtering	RT	
[26]	SnO	7.8	~1.7	$\sim2 \times 10^6$	ALD	150 ~ 210	
[27]	SnO	20	1.2	2.8×10^3	Sputtering	RT	
[28]	SnO	30	1.2	7.3×10^3	Sputtering	RT	La doping

[29]	SnO	20	1.0	5×10^{4}	Sputtering	RT	Ambipolar
[30]	SnSeO	30	5.9	3×10^{2}	Sputtering	RT	
[31]	CuI	5 ~ 8	1.9	~10^{2}	Solution	RT	Estimated $I_{ON/OFF}$ based on the corresponding reference
[32]	CuI	~10	4.4	~10^{7}	Solution	RT	Zn doping
[33]	CuI	~9	5.3	10^{6} ~ 10^{7}	Solution	RT	Zn doping
[34]	Te	16	~700	10^{2} ~ 10^{3}	Solution	RT	Estimated $I_{ON/OFF}$ based on the corresponding reference
[35]	Te	12.3	419	3×10^{3}	Solution	180	
[36]	Te	8	35	10^{4}	Evaporation	-80	
[37]	Te	7	50	10^{3} ~ 10^{4}	Evaporation	-80	Estimated $I_{ON/OFF}$ based on the corresponding reference
[38]	Te	13	~100	10^{4}	Solution	180	Nanowire; Estimated mobility based on the corresponding reference
[39]	Te	50	570	2×10^{4}	Solution	180	Dual-gated nanowire
[40]	Te	20	4.7	1×10^{4}	Solution	160	
[41]	Te	4	30	6×10^{5}	Evaporation	-80	Measured in vacuum environment
This work	Te	4	30.9	5.8×10^{5}	Sputtering	RT	

*)Fab. Temp. indicates the temperature during the fabrication of channel material.

Supplementary References

1. Kingery, W. D., Bowen, H. K. & Uhlmann, D. R. *Inroduction to Ceramics* 2nd edn (Wiley, New York, 1975).
2. Fujihara, S., Sasaki, C. & Kimura, T. Crystallization behaviour and origin of c-axis orientation in sol-gel-derived ZnO:Li thin films on glass substrates. *Appl. Surf. Sci.* **180**, 341-350 (2001).
3. Aspiala, M., Sukhomlinov, M. & Taskinen, P. Standard Gibbs energy of formation of tellurium dioxide measurement by a solid-oxide electrolyte EMF technique. *Thermochim. Acta* **573**, 95-100 (2013).
4. Yim, K. et al. Computational discovery of p-type transparent oxide semiconductors using hydrogen descriptor. *Npj Comput. Mater.* **4**, 17 (2018).
5. Li, L. et al. Black phosphorous field-effect transistors. *Nat. Nanotech.* **9**, 372-377 (2014).
6. Zhu, W. et al. Flexible black phosphorus ambipolar transistors, circuits and AM demodulator. *Nano Lett.* **15**, 1883 (2015).
7. Liu, H. et al. Phosphorene: an unexplored 2D semiconductor with a high hole mobility. *ACS Nano* **8**, 4033 (2014).
8. Das, S. et al. Ambipolar phosphorene field effect transistor. *ACS Nano* **8**, 11730 (2014).
9. Liu, H. et al. The effect of dielectric capping on few-layer phosphorene transistors: Tuning the Schottky barrier heights. *IEEE Electron Device Lett.* **35**, 795 (2014).
10. Li, L. et al. High-performance p-type black phosphorus transistor with scandium contact. *ACS Nano* **10**, 4672 (2016).

11. Liu, X. et al. Black phosphorus based field effect transistors with simultaneously achieved near ideal subthreshold swing and high hole mobility at room temperature. *Sci. Rep.* **6**, 24920 (2016).

12. Pradhan, N. R. et al. Field-Effect Transistors Based on Few-Layered α-$MoTe_2$. *ACS Nano* **8**, 5911 (2014).

13. Zhou, L. et al. Large-Area Synthesis of High-Quality Uniform Few-Layer $MoTe_2$. *J. Am. Chem. Soc.* **137**, 11892 (2015).

14. Lin, Y.-F. et al. Ambipolar $MoTe_2$ Transistors and Their Applications in Logic Circuits. *Adv. Mater.* **26**, 3263 (2014).

15. Fathipour, S. et al. Exfoliated multilayer $MoTe_2$ field-effect transistors. *Appl. Phys. Lett.* **105**, 192101 (2014).

16. Qu, D. et al. Carrier-Type Modulation and Mobility Improvement of Thin $MoTe_2$. *Adv. Mater.* **29**, 1606433 (2017).

17. Liu, X. et al. P-Type Polar Transition of Chemically Doped Multilayer MoS_2 Transistor. *Adv. Mater.* **28**, 2345 (2016).

18. Zhang, S. et al. Improved contacts to p-type MoS_2 transistors by charge-transfer doping and contact engineering. *Appl. Phys. Lett.* **115**, 073106 (2019).

19. Ma, Z. et al. High Current Nb-Doped P-Channel MoS_2 Field-Effect Transistor Using Pt Contact. *IEEE Electron Device Lett.* **42**, 343-346 (2021).

20. Shokouh, S. H. H. et al. High-Performance, Air-Stable, Top-Gate, p-Channel WSe_2 Field-Effect Transistor with Fluoropolymer Buffer Layer. *Adv. Funct. Mater.* **25**, 7208 (2015).

21. Yu, L. et al. High-Performance WSe_2 Complementary Metal Oxide Semiconductor Technology and Integrated Circuit. *Nano Lett.* **15**, 4928 (2015).

22. Campbell, P. M. et al. Field-effect transistors based on wafer-scale, highly uniform few-layer p-type WSe_2. *Nanoscale* **8**, 2268 (2016).

23. Bae, J. H. et al. Gallium doping effects for improving switching performance of p-type copper (I) oxide thin-film transistors. *ACS Appl. Mater. Interfaces* **12**, 38350 (2020).

24. Chang, H. et al. Back-Channel Defect Termination by Sulfur for p-Channel Cu_2O Thin-Film Transistors. *ACS Appl. Mater. Interfaces* **12**, 51581 (2020).

25. Min, W. K. et al. Switching Enhancement via a Back-Channel Phase-Controlling Layer for p-Type Copper Oxide Thin-Film Transistors. *ACS Appl. Mater. Interfaces* **12**, 24929 (2020).

26. Kim, S. H. et al. Fabrication of high-performance p-type thin film transistors using atomic-layer-deposited SnO films. *J. Mater. Chem. C* **5**, 3139 (2017).

27. Kim, T. et al. Improved switching characteristics of p-type tin monoxide field-effect transistors through Schottky energy barrier engineering. *J. Mater. Chem. C* **8**, 201 (2020).

28. Yim, S. et al. Lanthanum Doping Enabling High Drain Current Modulation in a p-Type Tin Monoxide Thin-Film Transistor. *ACS Appl. Mater. Interfaces* **11**, 47025 (2019).

29. Kim, T. et al. Origin of Ambipolar Behavior in p-Type Tin Monoxide Semiconductors: Impact of Oxygen Vacancy Defects. *IEEE Trans. Electron Devices* **68**, 4467 (2021).

30. Kim, T. et al. Material Design of New p-Type Tin Oxyselenide Semiconductor through Valence Band Engineering and Its Device Application. *ACS Appl. Mater. Interfaces* **11**, 40214 (2019).

31. Liu, A. et al. Room-Temperature Solution-Synthesized p-Type Copper (I) Iodide Semiconductors for Transparent Thin-Film Transistors and Complementary Electronics. *Adv. Mater.* **30**, 1802379 (2018).

32. Liu, A. et al. Key Roles of Trace Oxygen Treatment for High-Performance Zn-Doped CuI p-Channel Transistors. *Adv. Electron. Mater.* **7**, 2000933 (2021).

33. Liu, A. et al. High-performance p-channel transistors with transparent Zn doped-CuI. *Nat. Commun.* **11**, 4309 (2020).

34. Wang, Y. et al. Field-effect transistors made from solution-grown two-dimensional tellurene. *Nat. Electron.* **1**, 228-236 (2018).

35. Amani, M. et al. Solution-synthesized high-mobility tellurium nanoflakes for short-wave infrared photodetectors. *ACS Nano* **12**, 7253-7263 (2018).

36. Zhao, C. et al. Evaporated tellurium thin films for p-type field-effect transistors and circuits.*Nat. Nanotech.* **15**, 53-58 (2020).

37. Zhao, C. et al. Thermal stability for Te-based devices. *Appl. Phys. Lett.* **117**, 192104 (2020).

38. Qin, J.-K. et al. Raman response and transport properties of tellurium atomic chains encapsulated in nanotubes. *Nat. Electron.* **3**, 141-147 (2020).

39. Dasika, P. et al. Contact-Barrier Free, High Mobility, Dual-Gated Junctionless Transistor Using Tellurium Nanowire. *Adv. Funct. Mater.* **31**, 2006278 (2021).

40. Naqi, M. et al. Nanonet: Low-temperature-processed tellurium nanowire network for scalable p-type field-effect transistors and a highly sensitive phototransistor array. *NPG Asia Mater.* **13**, 46 (2021).

41. Zhao, C. et al. Tellurium Single-Crystal Arrays by Low-Temperature Evaporation and

Crystallization. *Adv. Mater.* **33**, 2100860 (2021).